Fabrication and interfacial characterization of Ni-rich thin-film cathodes for stable Li-ion batteries

Ming Jiang [a,b,c,1], Xiaochao Wu [d,1], Qian Zhang [b,d,1], Dmitri L. Danilov [a,b], Rüdiger-A. Eichel [b,d], Peter H.L. Notten [a,b,e,*]

[a] Eindhoven University of Technology, P.O. Box 513, 5600 MB, Eindhoven, the Netherlands
[b] IEK-9, Forschungszentrum Jülich, Jülich D-52425, Germany
[c] SVOLT Energy Technology Co., Ltd. Wuxi City 1066, China
[d] RWTH Aachen University, Aachen D-52074, Germany
[e] University of Technology Sydney, Broadway, Sydney, NSW 2007, Australia

ARTICLE INFO

ABSTRACT

Ni-rich $LiNi_{0.6}Co_{0.2}Mn_{0.2}O_2$ (NCM) and $LiNbO_3$-protected $LiNi_{0.6}Co_{0.2}Mn_{0.2}O_2$ (NCM) thin-film cathodes have been prepared by radio frequency (RF) magnetron sputtering. Electrochemical investigations show enhanced stability of $LiNbO_3$-protected cathodes compared with bare $LiNi_{0.6}Co_{0.2}Mn_{0.2}O_2$. The interfacial interaction of $LiNbO_3$ and $LiNi_{0.6}Co_{0.2}Mn_{0.2}O_2$ layers has been investigated by XPS depth profiling and demonstrated different cathode electrolyte interface (CEI) film formation processes at the electrodes. The results elaborate on the interaction between $LiNbO_3$ and $LiNi_{0.6}Co_{0.2}Mn_{0.2}O_2$, emphasizing the role of the $LiNbO_3$ layer in improving the cycling performance of Ni-rich cathodes.

1. Introduction

Rechargeable lithium-ion batteries (LIBs) have undoubtedly become one of the most powerful energy storage devices upon intensive studies for decades. They have been successfully applied in various fields, such as portable devices, electric vehicles, and large-scale energy systems [1]. Over the last decades, wide-ranging research has been pursuing battery systems with higher energy density, higher safety, and lower cost for meeting the increasing demands of LIBs [2,3]. Cathode materials are considered the bottleneck for further improving the battery performance to the next level. Among all sorts of cathode materials, Ni-rich layered transition metal oxide $LiNi_xCo_yMn_zO_2$ ($x > 0.6$) has shown the largest commercial interest as an alternative to $LiCoO_2$, owing to its demonstrated high capacity of up to ~200mAh/g. Despite a promising high energy density, Ni-rich cathodes are not yet very stable compared with other conventional cathodes ($LiCoO_2$, $LiMnO_2$, $LiFePO_4$) [4,5]. Ni-rich cathode suffers from several de-

ficiencies, including transition metal dissolution, surface phase transformation from layered to inactive rock-salt structure, and residuals adhered on the electrode caused by electrolyte decomposition [6,7]. All side products comprise of a cathode electrolyte interface (CEI) film on the electrode/electrolyte interface, which dramatically increases the system impedance and can be detrimental to battery performance and lifetime [8].

Many candidates have been introduced as protective layers to stabilize the CEI film on Ni-rich cathodes. One can mention metal oxides (Al_2O_3, TiO_2, MgO, etc.) [9–11], metal fluorides (AlF_3, LiF, etc.) [12,13], solid-state electrolytes (Li_3PO_4, Li_2ZrO_3, etc.) [14–16], carbon (e.g. graphene, CNT) and polymers [17–20]. However, most materials are Li-ion insulators with extremely low Li-ion diffusion coefficients, leading to low initial discharge capacities. Good Li-ion conductors, such as the solid-state electrolytes, can efficiently alleviate electrode degradation by suppressing the CEI film formation and providing facile Li-ion transportation across the interface. Lithium niobate ($LiNbO_3$), a solid-state electrolyte with high ionic conductivity and a relatively wide electrochemical stability window, has been applied as a coating layer on other cathode materials ($LiCoO_2$, $LiMn_2O_4$, $LiNi_{0.5}Mn_{1.5}O_4$) [21–23]. However, the combination of $LiNbO_3$ and Ni-rich cathode is rarely reported in the

---

literature. The mechanism behind the improved performance of LiNbO$_3$-coated Ni-rich cathode remains unclear, and the interaction between layers was neither studied.

Additionally, existing research has recognized that additives used in conventional powder electrodes, such as conductive carbon and PVDF binder, also play a critical role in the CEI and SEI film formation at cathodes and anodes, respectively [24,25]. The contributions from these additives are likely to obscure reactions between the electrodes and electrolytes, making it essential to fabricate a simplified system to fundamentally study the electrode degradation mechanisms. Thin-film electrodes can provide a simple electrode configuration to study interfacial phenomena by isolating the additives from the electrodes and electrolytes. Another feature of the thin-film electrodes is the highly homogeneous morphology, which offers a clean and identical sample surface for analyses. Recently, several reports described thin-film electrodes for interfacial investigations. Still, the study in LiNbO$_3$/Ni-rich cathode thin-film electrode system has not been reported before [26–29].

In this work, we fabricated LiNi$_{0.6}$Co$_{0.2}$Mn$_{0.2}$O$_2$ cathodes (bare-NCM) and LiNbO$_3$-coated LiNi$_{0.6}$Co$_{0.2}$Mn$_{0.2}$O$_2$ cathodes (LiNbO$_3$@NCM) by radio frequency (RF) magnetron sputtering. Clearly enhanced electrochemical performance was obtained with LiNbO$_3$-protected electrodes. The interaction between NCM and LiNbO$_3$ and CEI film formation mechanism between the electrodes and electrolyte are also illustrated.

2. Experimental

2.1. Synthesis

All sputter deposition targets were obtained from Advanced Engineering Materials Co., Ltd., China. Silicon wafers and quartz wafers with 3′ diameters were used as substrates. The Physical Vapor Deposition (PVD) machine (Kurt J. Lesker, UK) was used to prepare the samples. The current collector was deposited by direct-current (DC) magnetron sputtering of Pt onto the Si substrates. Thin-film electrodes were prepared by radio-frequency (RF) magnetron sputtering, combined with post-annealing. The sputtering process was performed in an Ar atmosphere under the chamber pressure of 5 mTorr and the sputtering power of 70 W. After deposition the thin-film samples were annealed in air at either 300, 400 or 500 °C.

2.2. Characterization

Scanning electron microscopy (SEM) images were taken on a Quanta FEG 650 (FEI, USA) environmental scanning electron microscope operated at a voltage of 20 kV. X-ray diffraction (XRD) measurements were performed between 10° and 80° using Cu Kα radiation using an EMPYREAN X-ray diffractometer (Panalytical, The Netherlands). Inductively Coupled Plasma Source Mass Spectrometry (ICP-MS) was analyzed by the Agilent 7900 ICP-MS (Agilent, USA). X-ray photoelectron spectroscopy (XPS) was performed by a Thermo Scientific K-Alpha instrument with a monochromatic X-ray source (Al Kα), and depth profiling was carried out by a 500eV gas cluster ion source beam.

2.3. Electrochemical measurements

The electrochemical performance was tested in homemade Teflon cells; the schematic configuration can be found in our previous publication [30]. The surface area for both thin-film samples was 1.54 cm^2. Metallic lithium metal was used as both counter and reference electrodes. 1 M LiPF$_6$ in a 1:1 mixed solvent of ethylene carbonate (EC)/dimethylcarbonate (DMC) (LP30, BASF, USA) was used as an electrolyte. All electrochemical tests were performed in

an Ar-filled glovebox using an M2300 galvanostat (Maccor, USA). Galvanostatic charge/discharge cycling was operated in the voltage range of 3.0−4.1 V *vs.* Li/Li$^+$. Electrochemical impedance spectroscopic (EIS) investigations were conducted by an Autolab PGSTAT 302 (Metrohm-Autolab B.V., The Netherlands) with an amplitude of 5 mV in the frequency range from 0.1 Hz to 1 MHz. EIS fitting process was performed in Zview®.

3. Results and discussion

Ni-rich LiNi$_{0.6}$Co$_{0.2}$Mn$_{0.2}$O$_2$ thin-films were deposited using a Li$_{1.1}$Ni$_{0.6}$Co$_{0.2}$Mn$_{0.2}$O$_2$ ceramic target. Excess of Li was used to compensate for Li losses during sputtering and subsequent annealing. SEM images and corresponding EDX elemental mapping analyses of the annealed- LiNi$_{0.6}$Co$_{0.2}$Mn$_{0.2}$O$_2$ (NCM) thin-film samples deposited on Si substrate are shown in Fig. 1. Compared with the as-deposited NCM films (Fig. S1), the thin film surface after high-temperature annealing presents a relatively rough morphology, with small sphere-like aggregated particles (Fig. 1a). The EDX elemental analysis shows a uniform elemental distribution for the crystallized NCM film (Fig. 1c). It reveals that the Ni:Co:Mn atomic ratio is 17.64:6.32:5.78, consistent with the NCM sputtering target's elemental ratio. Similar to the pure NCM film, the surface of LiNbO$_3$@NCM film shows the nano-sized crystalline grains (Fig. 1d). The cross-section view of the film is given in Fig. 1e. The thickness of NCM and LiNbO$_3$ layers are 200 and 300 nm, respectively. The interfacial contact between the layers is found to be compact. The elemental distribution of Nb and O in the LiNbO$_3$@NCM thin film has also been examined by EDX measurements (Fig. 1f). The atomic ratio between Nb and O (22.07:77.93) is similar to that of the LiNbO$_3$ target. Note that EDX of active electrode materials often shows some unlabeled peaks related to the elements in the substrate, the adhesive layer, barrier layer, and current collector. In the present study, the irrelevant elements are excluded, and a precise elemental ratio of active material is obtained.

XRD was employed to compare the crystal structure of the as-prepared films under various annealing temperatures to determine the most optimized crystallization conditions. The diffraction patterns of the as-deposited NCM film and samples post-annealed at 300, 400, and 500 °C in Fig. 2a indicate a structural transformation from the amorphous phase to the crystalline structure with the sharpest peaks at the highest temperature. Compared to the standard LiNiO$_2$ hexagonal layered structure (R-3m space group), the samples annealed at 400 and 500 °C are in good agreement with the reference material. Notably, the film annealed at 500 °C displays more distinct (101) and (104) reflections than the 400 °C annealed film. It has been proven that Li-ion transportation takes place along the (101) and (104) planes, while it is impeded along the (003) plane [29]. Therefore, post-annealing NCM thin films at 500 °C were further applied in all experiments. In addition, LiNbO$_3$ thin-films prepared under various annealing temperatures have been XRD analyzed in detail. As shown in Fig. 2b, the as-deposited LiNbO$_3$ presents an amorphous structure. However, with increasing annealing temperature, the crystallinity of the thin film was significantly enhanced. The characteristic peaks of the 400 and 500 °C annealed films correspond nicely to the standard hexagonal LiNbO$_3$ structure (R3cH space group). Considering that the NCM layer was annealed at 500 °C, the heating process for the LiNbO$_3$ layer applied at 400 °C will not influence the crystallinity of NCM.

A series of electrochemical examinations were carried out on LiNbO$_3$ thin films to probe its feasibility as a solid-state electrolyte. The stability window of annealed LiNbO$_3$ film was investigated, as shown in Fig. S2a (the liquid electrolyte used in the measurement is 1M LiPF$_6$, EC/DMC 1:1), and one reversible redox couple was found at 2.6 and 3.7 V in the cyclovoltammogram (CV). In contrast to the amorphous LiNbO$_3$ film, the annealed sample is
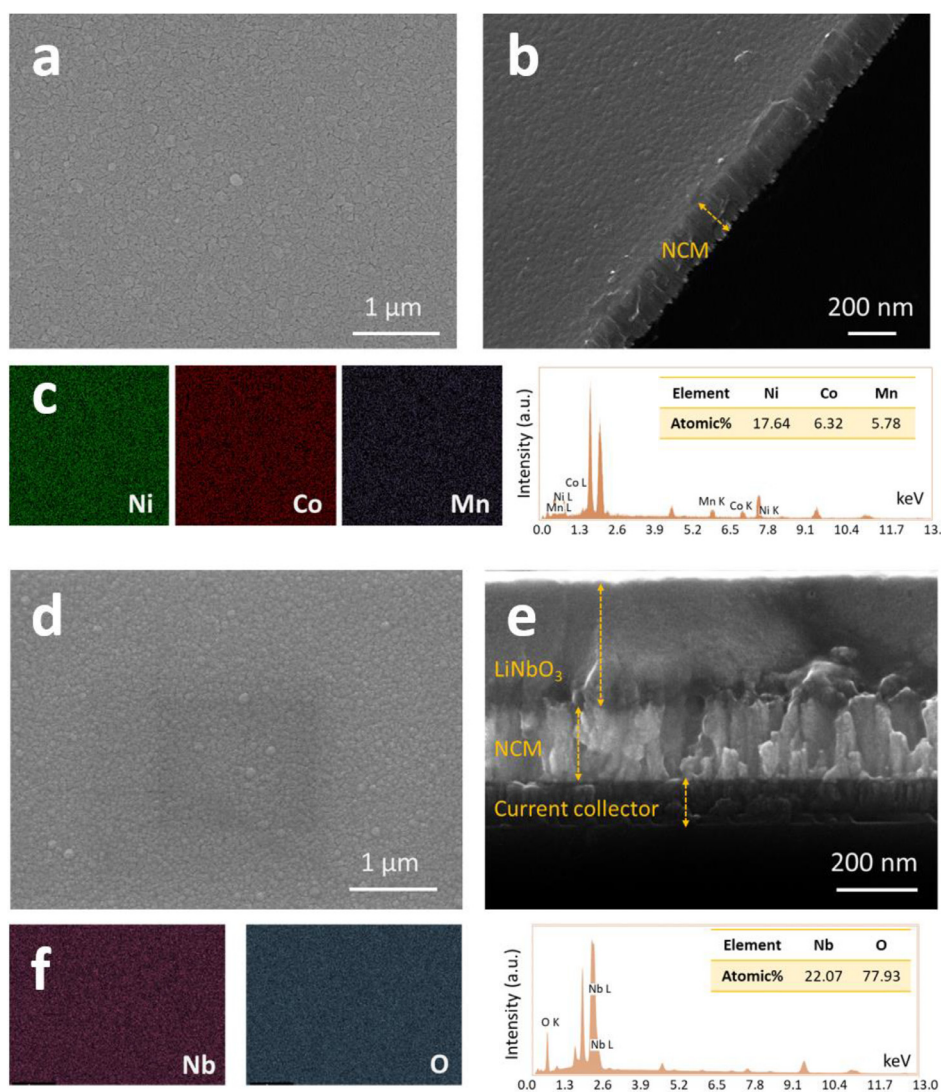
Fig. 1. SEM image of (a) bare-NCM thin-film and (d) LiNbO₃@NCM thin-film; Cross-sectional SEM image of (b) bare-NCM thin-film and (e) LiNbO₃@NCM thin-film; EDX elemental analysis of (c) bare-NCM thin-film and (f) LiNbO₃@NCM thin-film.

more stable with a stability window ranging from approximately 2.0 to 4.2 V, comparable with what has been reported in the literature [31,32]. Impedance measurements are made on a sandwich-structure Pt/LiNbO₃/Pt electrode to investigate the ionic conductivity, as shown in Fig. S2b. The area and thickness of each microelectrode are 1×1 cm^2 and 300 nm, respectively. The result reflects that the annealed film delivered a higher Li-ion conductivity $(1.32 \bullet 10^{-5}$ S cm$^{-1})$ at room temperature, compared to the amorphous films $(3.47 \bullet 10^{-7}$ S cm^{-1} in Fig. S2c and 2d).

The effect of the LiNbO₃ layer coating on NCM cathodes is further investigated by XPS depth profiling analysis. Multiple signals were collected after sputtering with Ar500+ cluster ion source for 80 s for each collection. The evolution of the Ni 2p, Co 2p, Mn 2p, Nb 3d, and O 1s reflections for a bare-NCM film and a LiNbO₃@NCM electrode are shown in Figs. 3 and S3. In the Ni 2p spectra (Fig. 3a), two characteristic peaks located at 855.8 and 862.5 eV are corresponding with the binding energy of Ni^{3+} 2p$_{3/2}$ and Ni 2p$_{1/2}$, respectively. The elemental valence of Ni in the bare-NCM film remains consistent along with the increasing sputtering depth. In Fig. 3b, two peaks of O 1s spectra are assigned to the bonding energy in M-O (M=Ni, Co, Mn; 529.1 eV) and Li₂CO₃ (or LiOH; 532.2 eV). The existence of Li₂CO₃ (or LiOH) is resulting from the chemically adsorbed species. This phenomenon has been com-

monly observed in the XPS spectra of Ni-rich cathode materials [12]. The sample was prepared in the open air. Thus a higher content of adsorbed species was found at the sample surface, leading to a higher intensity of the Li₂CO₃ (or LiOH) peak on the first sputtering layer [33].

The XPS depth profiles obtained with the LiNbO₃@NCM thin-film give an interesting observation of the NCM/LiNbO₃ interface. In Fig. 3c, the evolution of Ni 2p spectra reveals a gradual valence change at the NCM/LiNbO₃ interface. The O spectra of LiNbO₃@NCM thin-film also present the transition from the LiNbO₃ layer (single peak located at 530.8 eV) to the NCM layer (two peaks). In addition, the Nb 3d spectra extracted from LiNbO₃@NCM thin-film display the valence evolution as well (Fig. S3e). However, for Co and Mn, both thin films showed identical elemental valences, and apparently, no valence state changes can be found at the interface. In Fig. S3a and S3c, the dominant valence of Co is Co^{3+} and is represented by a strong peak at 779.5 eV. For the Mn spectra, the binding energy of 641.9 eV indicates that the Mn ions mainly exist as tetravalent in as-prepared NCM film (Fig. S3b and S3d). The results obtained on NCM films match well with the NCM samples prepared by other synthesis methods.[34] The corresponding Ni 2p, Nb 3d, and O 1s spectra at the NCM/LiNbO₃ interface are summarized in Fig. 4.
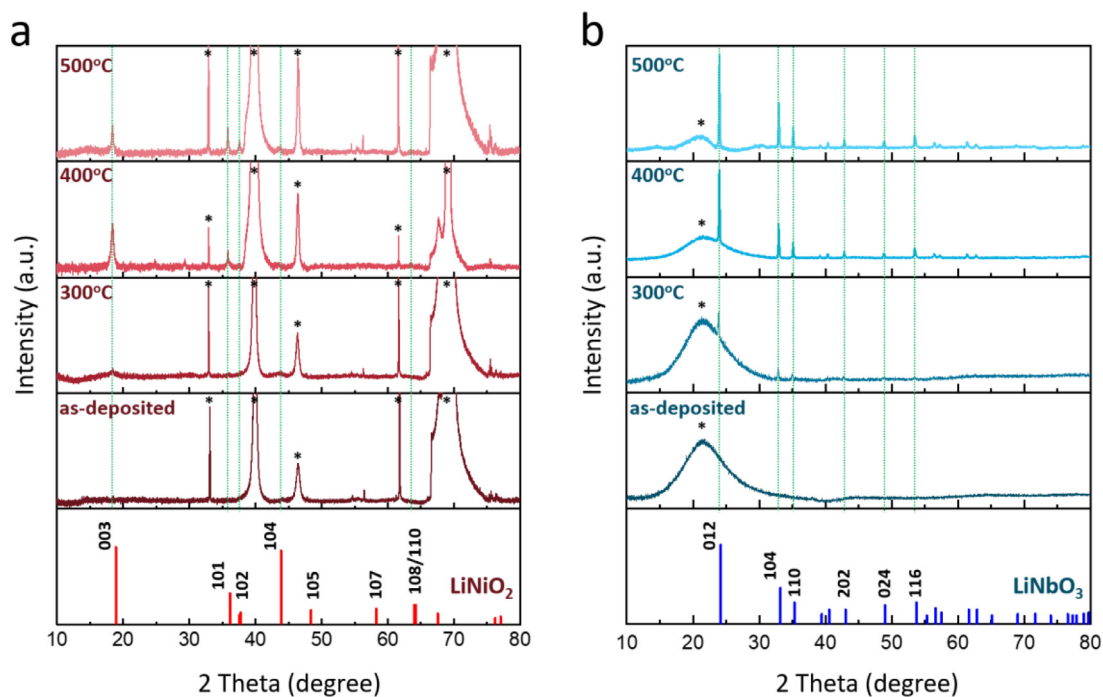
Fig. 2. XRD patterns of (a) NCM thin-film and (b) LiNbO$_3$ thin-film under different annealing conditions. The peaks marked with a black asterisk are related to the substrates. Silicon and quartz wafers were used as substrates for the XRD measurements of NCM and LiNbO$_3$ thin films, respectively. The broad peak of the quartz wafers will overlap with the characterized (003) reflection of NCM thin-film. Thus silicon wafer was used in the XRD measurement of NCM thin films.
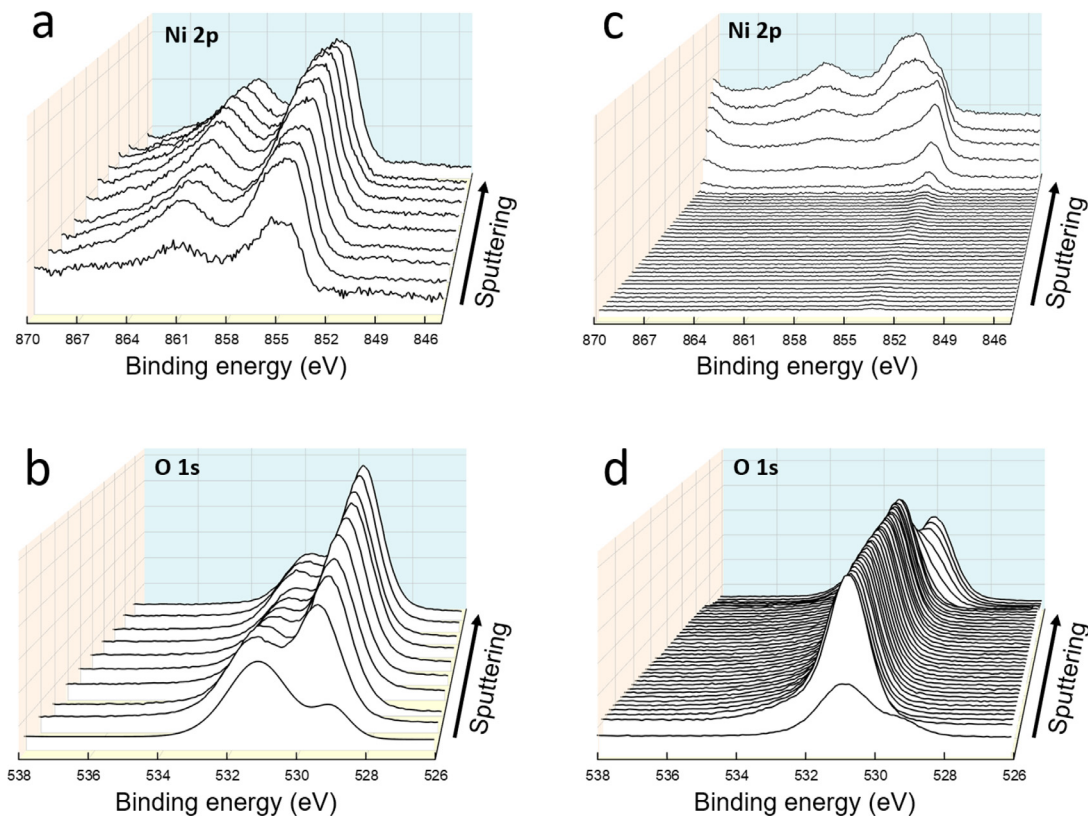

Fig. 3. XPS depth profiling of a pristine bare-NCM thin-film for (a) Ni 2p, (b) O 1s, and a pristine LiNbO$_3$@NCM thin-film for (c) Ni 2p, (d) O 1s spectra.
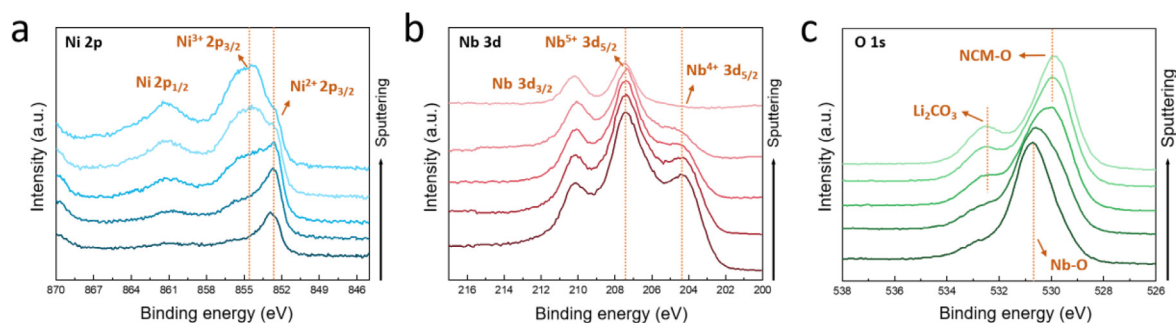
Fig. 4. XPS spectra of (a) Ni 2p, (b) Nb 3d, and (c) O 1s XPS spectra extracted from the $LiNbO_3$/NCM interface.

As displayed in Fig. 4, the spectra of Ni 2p, Nb 3d, and O 1s along the depth direction from the $LiNbO_3$ top layer towards the underlying NCM layer are extracted. Fig. 4a shows the Ni that existed in the interlayer as Ni^{2+} ions. The intensity of Ni^{2+} $2p_{3/2}$ peak (853.6 eV) increased while the etching process approaching the NCM layer, and the dominant valence state of Ni ion gradually transferred into Ni^{3+} (855.8 eV), consistent with the chemical environment in pure NCM material. Accordingly, the spectra of Nb 3d presents Nb^{5+} $3d_{5/2}$ (207.1 eV) on the $LiNbO_3$ surface, while the co-existence of Nb^{5+} $3d_{5/2}$ and Nb^{4+} $3d_{5/2}$ peaks (204.2 eV) in the bulk of the $LiNbO_3$ layer (Fig. S4). This can be explained by insufficient oxygen exposure to $LiNbO_3$ during the heat treatment; the structure of the as-deposited layer is highly compact. The Nb^{4+} peak intensity decreased in the interface layer and eventually became undetectable along with an increasing sputtering depth (Fig. 4b).

The evolution of Nb^{4+} when approaching the NCM layer is related to the escalating influence of Ni ion on Nb species. Ni reveals a much stronger electronegativity than Nb [35]. Thus, the electronic cloud of Nb^{4+} was polarized toward Ni ions, resulting in the raised valence state of Nb^{4+}. The lattice oxygen releasing from the NCM layer surface may also oxidize Nb^{4+} into Nb^{5+} in the interface area. In addition, O 1s spectra at the interface show the correlative transformation as Ni 2p and Nb 3d (Fig. 4c). The single sharp peak located at 530.8 eV demonstrated the O element at the interface is mainly from Nb-O. With the increasing depth, the O 1s spectra are gradually dominated by the O species from NCM material (M-O, M=Ni, Co, Mn). As discussed before, a small peak observed at 532.2 eV was attributed to chemically adsorbed oxygenic species (Li_2CO_3 or LiOH), displaying an identical characteristic peak as the O spectra obtained for pure NCM films. In short, the interphase between NCM and $LiNbO_3$ layers formed during the heat treatment in the preparation process is associated with Ni ion diffusion and interaction with the $LiNbO_3$ films. Moreover, based on the XPS depth profiling analyses, the intrinsic thickness of the interface is analyzed at approximately 30 nm.

The electrochemical properties of the as-obtained thin-film electrodes are shown in Fig. 5 within a voltage range of 3.0 to 4.1 V (*vs.* Li/Li$^+$). As a reference, the performance of a commercial $LiNi_{0.6}Co_{0.2}Mn_{0.2}O_2$ powder electrode is also included in Fig. 5a and b. The characteristic sloping voltage regions for thin-film electrodes can be found in the (dis)charge curves and are comparable to that for an NCM powder electrode. Obviously, the discharge specific capacity of the thin-film electrodes is somewhat lower than that of the commercial powder electrode. A probable explanation is that the thin-film electrode configuration is restricted by its contact area with electrolyte. Consequently, the electrochemical reaction of active material is somewhat hampered during operation. A similar phenomenon has been reported in other work [25]. Nevertheless, the $LiNbO_3$-coated sample demonstrates an improved specific discharge capacity (161.4 mAh g^{-1}) in comparison to the bare

NCM thin-film (157.5 mAh g^{-1}) (Fig. 5a). Fig. 5b shows the differential capacity (dQ/dV) plot of all electrodes obtained from Fig. 5a. Two oxidation peaks appeared during the deintercalation process, revealing the identical phase transition for all electrodes. According to the previous research, these two peaks can be identified as phase transformation from hexagonal (H1) to monoclinic (M) and monoclinic to hexagonal (H2) in Ni-rich cathodes.[36,37] These results indicate that the thin films underwent the same phase transformation process as powder electrodes.

The cycling stability of thin-film electrodes during the first 30 cycles is shown in Fig. 5c. For the $LiNbO_3$-protected NCM thin-film, it can be seen that the initial discharge capacity and coulombic efficiencies are higher than those of the bare-NCM thin-film electrode. The discharge capacity of both films is declining upon cycling, whereas the bare-NCM film exhibited a faster fading rate. Its capacity dropped 51.8% and can only deliver approximately 58.1 mAh g^{-1} after 30 cycles. On the other hand, the specific capacity of $LiNbO_3$@NCM film retained 84.1% and revealed 119.2 mAh g^{-1} at the end of cycling. Furthermore, the $LiNbO_3$@NCM film demonstrated an enhanced and steady coulombic efficiency (above 90%) compared to bare NCM film of around 80%. The continuous decay of coulombic efficiency for the bare-NCM film suggests degradation of its reversible specific capacity during operation.

The electrochemical impedance of both thin-film electrodes before and after cycling is shown in Fig. 5d. The Nyquist plots show a semicircle in the high frequency and a straight line at low frequencies, representing the charge transfer resistance (R_{ct}) and Li-ion diffusion, respectively. The fitting parameters of ohmic resistance (R_E) and Rct for electrodes are presented in Table S1. For the pristine samples, the bare-NCM reveals a low R_{ct} value of 11.4 Ω, while the R_{ct} of $LiNbO_3$@NCM sample shows an impedance of 93.5 Ω owing to the increase of layer thickness. However, after cycling, the initial resistance value of bare-NCM shown a significant increase and rise to 77.1 Ω. In contrast, the $LiNbO_3$@NCM shown a modest rise in R_{ct} to 115.1 Ω. Such behavior implies that the electrochemical kinetics of the bare-NCM sample was significantly hindered over time, suggesting some inactive species might agglomerate on the electrode surface.

To further investigate the electrode properties after cycling, SEM and EDX were applied to explore electrode surface morphological and elemental evolution. In Fig. S5, the bare-NCM film's surface exhibited a destructive morphology with several cracks. It is considered to be induced by volume changes of the Ni-rich cathode induced by cycling. The electrolyte could penetrate through the cracks during cycling and give rise to renewed CEI-formation of freshly exposed material. As discussed above, the existence of CEI is generally seen as a factor strongly related to the capacity deterioration of Ni-rich cathodes. In comparison, the morphology of cycled $LiNbO_3$@NCM thin-film electrodes presented a relatively intact structure. The $LiNbO_3$ layer tends to protect the underlying NCM layer from structural collapse. The EDX results detected
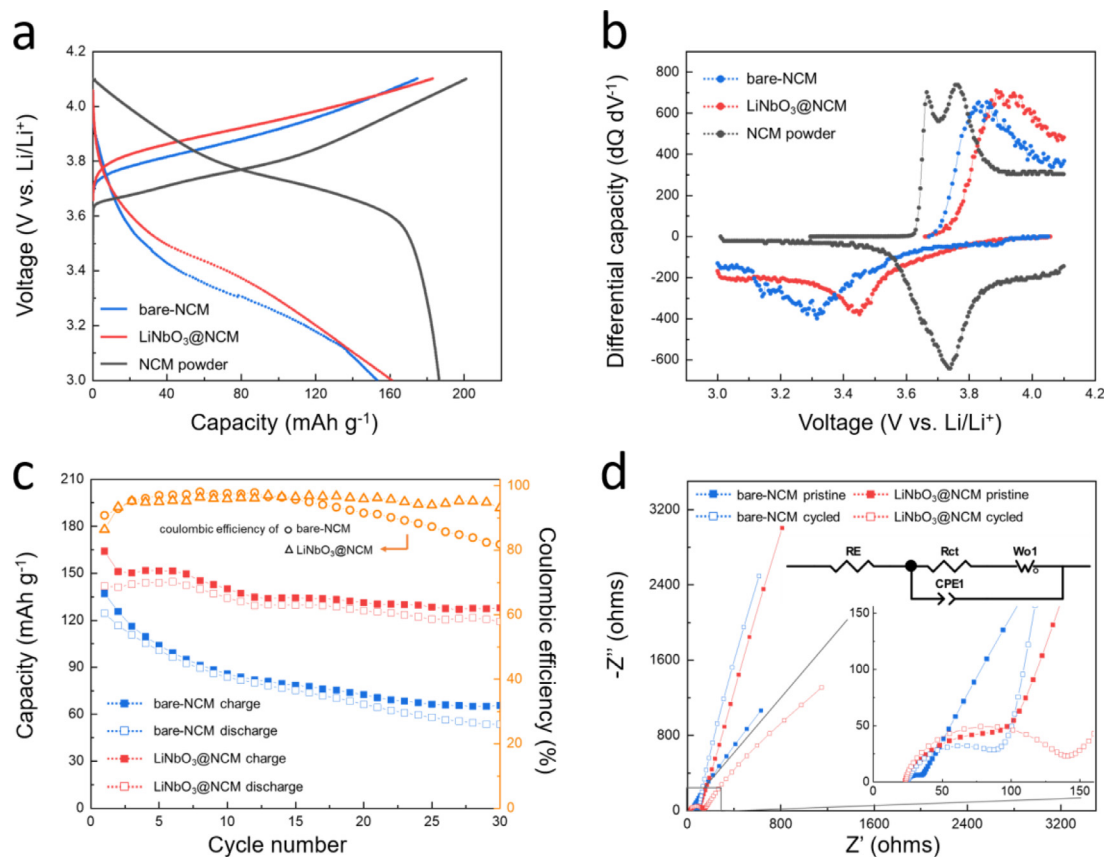
Fig. 5. (a) Constant current (dis)charge curves of thin-film and powder electrodes at 0.2 C-rate. (b) Differential capacity curves of the constant current curves of (a). (c) Cycling performance of thin-film electrodes at 0.5 C. (d) EIS plots of pristine and cycled electrodes.

P, and F-residuals at the surface, resulting from the CEI-formation. LiNbO$_3$@NCM films demonstrated a reduced P and F amount compared to bare-NCM thin films, suggesting a lower content of residuals formed at the electrode surface.

Most importantly, for Ni-rich cathode material, a relatively intact structure helps to survive HF attack from the electrolyte. HF is stemmed from the reaction between LiPF$_6$ salt and trace H$_2$O in the electrolyte, as described in reaction (1) [33,38].

$$LiPF_6 + H_2O \rightarrow LiF + POF_3 + HF \tag{1}$$

$$POF_3 + Li^+ + ne^- \rightarrow LiF + Li_xPO_yF_z \tag{2}$$
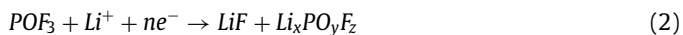
HF is highly toxic to most electrodes because HF tends to react with active material and leads to structural fatigue and transition metal dissolution. Regarding metal dissolution, it has been reported that nickel dissolution is one of the strongest degradation mechanisms of Ni-rich cathodes [39]. ICP test of the electrolyte after cycling is presented in Fig. S6 to evaluate the transition metal dissolution status for both electrodes. The result indicated that the LiNbO$_3$@NCM sample had a lower amount of dissolved metal ions than bare-NCM, showing the capability of the LiNbO$_3$ layer for inhibiting the transition metal dissolution caused by HF.

XPS depth profiling was again employed to allow a more in-depth insight into the chemical evolution of components in both thin films after cycling. For the bare-NCM electrode, as shown in Ni 2p spectra in Fig. 6a, the peaks on the first two layers are significantly different from those of pristine NCM film, indicating a Ni-consisted product generated on the surface. For the Co and Mn spectra, no such striking transformation can be observed along with the layer depth (Figures S7a and S7b). In the O 1s spectra (Fig. 6b), the peak development further revealed the complexity

of the chemical environment on the electrode surface. Moreover, P and F-contained residuals are detected that are generated in the relatively deeper layers inside the NCM film (Fig. 6c and d). The F 1s peak located at 685.1 eV is assigned to LiF, and the P 2p peak located at 135.0 eV is assigned to Li$_x$PO$_y$F$_z$. Both LiF and Li$_x$PO$_y$F$_z$ are decomposition products of LiPF$_6$ (reaction 2) and have been confirmed to be unfavorable to Li-ion transportation due to the high impedance [38,40]. Therefore, this finding suggests that the cracks on the cycled NCM film accelerate electrolyte penetration and the formation of undesirable reaction products.

XPS depth profiling of elements in LiNbO$_3$@NCM thin film is also demonstrated in Figs. 6 and S7. No noticeable evolution can be seen in the Ni 2p (Fig. 6e) and Nb 3d spectra (Fig. S7e) peaks compared with those of the pristine sample, suggesting the stability of the NCM/LiNbO$_3$ interface during the (dis)charge process. The valence state of O also displays a neglectable change after cycling (Fig. 6f). Similarly, Co 2p and Mn 2p spectra remained the relatively consistent chemical states after cycling (Figures S7c and S7d). In particular, according to the depth profiles of F 1s and P 2p, only the first few layers are found in which residuals of P, F-species can be found, implying the intact structure of LiNbO$_3$@NCM thin film (Fig. 6g and h). The lower content of LiF and Li$_x$PO$_y$F$_z$ at the electrode surface is associated with the fact that the LiNbO$_3$ layer significantly suppresses the decomposition of LiPF$_6$. Hence, one can conclude that the underlying NCM material was protected from electrolyte corrosion and that its electrochemical performance was less damaged than the bare-NCM thin-film electrode.

Subsequently, a more detailed analysis of the composition of CEI film generated at the electrode/electrolyte interface can be made. Figs. 7 and S8 provide the analysis of corresponding XPS spectra obtained from the surface of both thin films. For the bare-
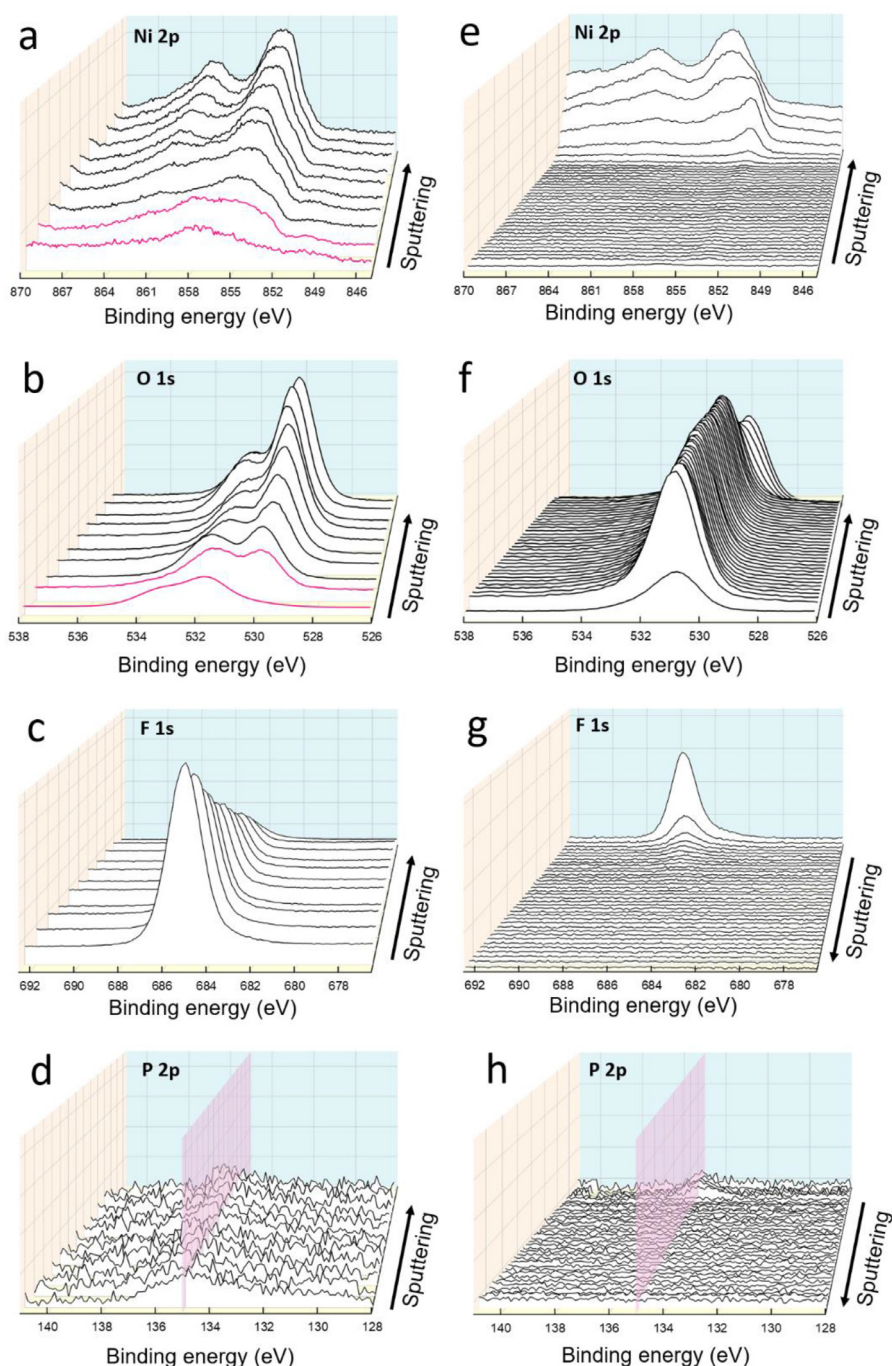
Fig. 6. XPS depth profiling analysis of the cycled bare-NCM thin-film for (a) Ni 2p, (b) O 1s, (c) F 1s (d) P 2p spectra, and cycled LiNbO$_3$@NCM thin-film for (a) Ni 2p, (b) O 1s, (c) F 1s (d) P 2p spectra. The red marked lines in panels (a) and (b) represent the existence of the NiO-type rock-salt layer. (For interpretation of the references to colour in their figure legend, the reader is referred to the web version of this article.)

NCM film, the Ni 2p spectra shown a rather complex development. As indicated in Fig. 7a, the initial Ni ion exited as Ni^{2+} (854.5 eV) and Ni^{3+} (855.2 eV) in the pristine electrode. While after cycling, three new Ni-contained phases can be found at the surface. The peak located at 861.2 eV is ascribed to NiO, resulting from the side reaction in the Ni-rich cathode, such as cation disorder during the (dis)charging [41]. In addition, the peak at 857.2 eV can be attributed to the binding energy of the Ni-F bond in NiF$_2$, which may be induced by the reaction between the dissolved Ni^{2+} ion and the decomposition products of LiPF$_6$: POF$_3$ and HF [42].

Moreover, a peak representing Ni^0 is also identified at 850.1 eV. A possible explanation of this is as follows: The dissolved Ni-ions

in the electrolyte reduce at the anode surface and form metallic Ni species. Then, the metallic Ni species partially transport from the anode side to the cathode surface during cycling. Recently, several reports have reported the chemical crossing of CEI/SEI components between the cathode and anode. These results indicate that the CEI is not only formed by electrolyte decomposition at the cathode surface but also the transportation of anodic components [43–45]. For example, Zhang *et al.* found that a modified separator can effectively suppress the chemical crossover from the anode to the cathode in a cycled LiFePO$_4$/Li cell [44]. Hamers et al. identified that the deposition of anodic species (LiP$_m$F$_p$O$_n$, C$_x$H$_y$O$_z$) at the LiNi$_{0.5}$Mn$_{0.3}$Co$_{0.2}$O$_2$ surface could be mitigated by using an Al$_2$O$_3$
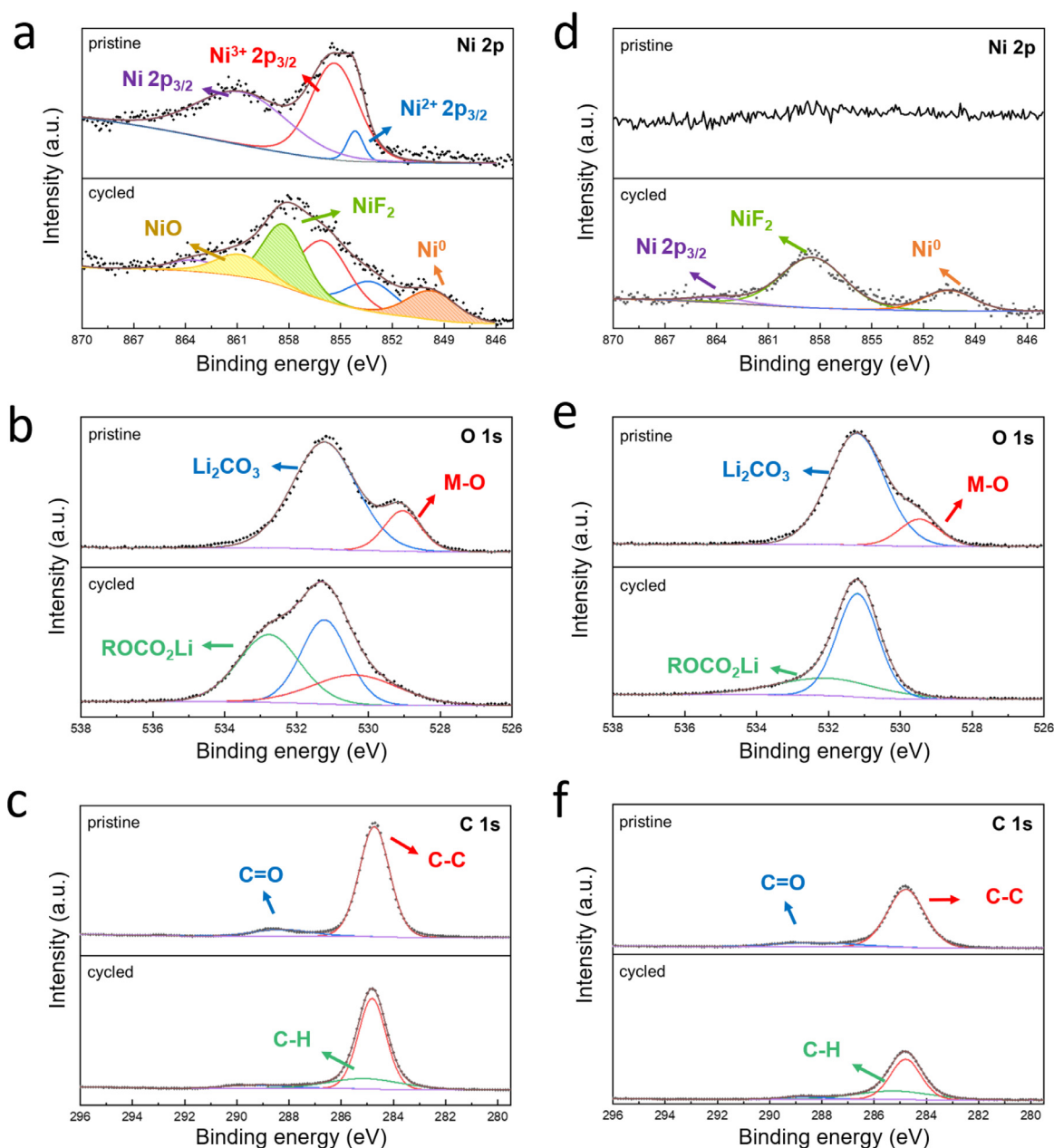
Fig. 7. XPS surface analysis of the pristine and cycled bare-NCM thin-film for (a) Ni 2p, (b) O 1s, (c) C 1s spectra, and the pristine and cycled LiNbO$_3$@NCM thin-film for (d) Ni 2p, (e) O 1s, (f) C 1s spectra.

cathode coating [43]. Other researchers also reported the presence of the Ni^0 signal in the XPS spectra at cycled cathode surfaces [46–48].

Fig. S8a and S8b display the Co and Mn spectra collected from the cycled bare-NCM electrode surface. With no new peaks found on both spectra, Co and Mn elements carried out a relatively stable behavior during cycling. In particular, the Mn 2p spectra has two major peaks located at 641.3 eV (representing Mn^{3+} 2p$_{3/2}$) and 642.4 eV (representing Mn^{4+} 2p$_{3/2}$). The content of Mn^{3+} 2p$_{3/2}$ increased slightly at the cycled electrode. The higher amount of Mn^{3+} results from the oxygen loss in the Ni-rich cathode when the surface structure transformed from layered to rock-salt phase. As-formed Mn^{3+} tends to partially reduce into Mn^{2+} and dissolve into the electrolyte, consequently declining the electrode's capacity to some extend [49].

The O 1s and C 1s spectra also provide information about the CEI component formed at the electrode surface. For the bare-NCM electrode before cycling (Fig. 7b), the dominant peaks are located at 529.0 and 531.1 eV. They can be associated with the M-O bond (M=metal) in NCM and C-O bond in Li$_2$CO$_3$, respectively. While after cycling, a relatively strong peak emerged at 533.7 eV, which can be ascribed to lithium alkyl carbonates (ROCO$_2$Li) [33,38]. Accordingly, in the C 1s spectra (Fig. 7c), two peaks can be detected for the pristine electrode. The peak at 584.8 eV is related to the C-C bond in the occasional carbon contamination. It has been confirmed that most samples that have been exposed to the atmosphere will have a detectable quantity of carbon on the surface [38]. The peak at 288.5 eV is the binding energy of O-C=O and should be attributed to Li$_2$CO$_3$. In cycled bare-NCM, a new peak located at 285.1 eV was identified, corresponding to the chemi-
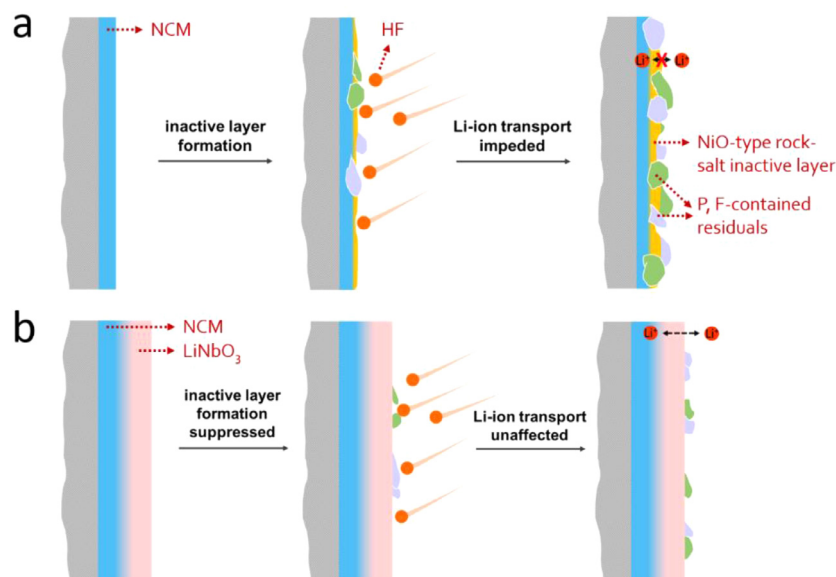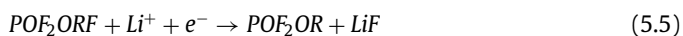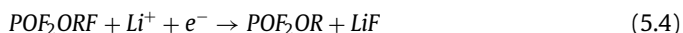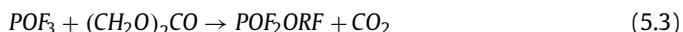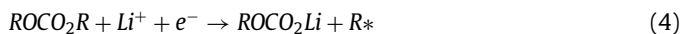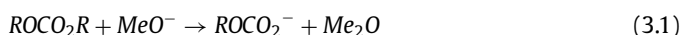
Fig. 8. Schematic diagram of the CEI film formation at bare-NCM (a) and LiNbO$_3$@NCM thin-film electrodes (b).

cal state C-O-C in ROCO$_2$Li. Although the generation mechanism of ROCO$_2$Li is remaining unclear, several different reaction routes have been proposed in previous reports: [50–53].

$$ROCO_2R + MeO^- \rightarrow ROCO_2^- + Me_2O \tag{3.1}$$

$$ROCO_2^- + Li^+ \rightarrow ROCO_2Li \tag{3.2}$$

$$ROCO_2R + Li^+ + e^- \rightarrow ROCO_2Li + R* \tag{4}$$

$$LiPF_6 \rightarrow LiF + PF_5 \tag{5.1}$$

$$PF_5 + ROH \rightarrow POF_3 + HF + RF \tag{5.2}$$

$$POF_3 + (CH_2O)_2CO \rightarrow POF_2ORF + CO_2 \tag{5.3}$$

$$POF_2ORF + Li^+ + e^- \rightarrow POF_2OR + LiF \tag{5.4}$$

$$POF_2ORF + Li^+ + e^- \rightarrow POF_2OR + LiF \tag{5.5}$$

On the other hand, for the LiNbO$_3$@NCM thin film electrode, the surface component development after cycling displayed a relatively different trend. In Fig. 7d, the Ni spectra inhibited two peaks at 850.1 eV and 861.2 eV, attributing to Ni-F bond in NiF$_2$ and Ni^0 2p$_{3/2}$, respectively. According to Fig. 7a, ions generated from dissolved Ni during cycling, the products of NiF$_2$ and metallic Ni are also formed at the LiNbO$_3$@NCM electrode surface, similar to the bare-NCM electrode. Meanwhile, Fig. S8c shows the XPS spectra of the Nb element, where a new peak located at 205.8 eV assigned to Nb^{4+} 3d$_{5/2}$ appearing at the cycled electrode. Accordingly, the presence of Nb^{4+} could be due to the reduction effect of metallic Ni towards Nb^{5+}. Likewise, regarding the O 1s and C 1s spectra (Fig. 7e and 7f, respectively), the characteristic peaks of Li$_2$CO$_3$ and ROCO$_2$Li were also found at the surface. However, compared with bare-NCM, the LiNbO$_3$@NCM electrode displayed a weaker peak intensity overall, especially for the ROCO$_2$Li component. This comparison suggests that the electrolyte decomposition and residuals formation on the electrode surface can be suppressed by the LiNbO$_3$ layer.

Based on XPS depth profiling and surface analysis, the chemical evolution of the CEI film at the electrode surface is illustrated in Fig. 8. For the bare-NCM electrode (Fig. 8a), an inactive NiO-like rock-phase layer triggered by cation-mixing and structural transition formed on the electrode surface during cycles. Meanwhile, the electrolyte component was decomposed and reacted on the electrode surface, creating various residuals, such as LiF, Li$_x$PO$_y$F$_z$, ROCO$_2$Li, *etc* [54–56]. On the other hand, the diffusing Ni-ions caused by the HF attack kept reacting with decomposition substances and turned into NiF$_2$. Notably, traces of P and F-containing residuals can be detected deeper inside the electrode, suggesting that the CEI film not only occurs at the electrode surface. It is mainly due to the growth of cracks and structural deterioration of the electrode, leading to a severe electrolyte penetration during cycling. As reported, most substances that consisted of CEI film (LiF, NiF$_2$, ROCO$_2$Li) are bad Li-ion conductors [33]. The relatively high impedance will hinder Li-ion transport, leading to fading of the electrochemical performance fading.

In contrast, the LiNbO$_3$@NCM electrode demonstrated the absence of a NiO-like layer on the NCM/LiNbO$_3$ interface. It contained fewer inactive products in the CEI film formed at the electrode surface (Fig. 8b). The inactive products only existed on the first few electrode layers, showing that the LiNbO$_3$ layer successfully prevented the underlying NCM material from electrolyte penetration and HF attack. The presented analyses indicate that the stability of the NCM/LiNbO$_3$ interface during cycling and the existence of the LiNbO$_3$ layer can effectively inhibit HF corrosion, suppress electrolyte decomposition, and eventually mitigate the CEI film growth.

4. Conclusions

LiNi$_{0.6}$Co$_{0.2}$Mn$_{0.2}$O$_2$ and LiNbO$_3$-coated LiNi$_{0.6}$Co$_{0.2}$Mn$_{0.2}$O$_2$ thin-film electrodes were fabricated via sputtering deposition on silicon substrates. Chemical and structural characterization revealed that the obtained films were of the desired crystallinity. XPS depth profiling was intensely applied to collect information from the LiNbO$_3$/LiNi$_{0.6}$Co$_{0.2}$Mn$_{0.2}$O$_2$ interface and CEI film formation at the electrodes. An interface with a thickness around 30 nm was identified between LiNi$_{0.6}$Co$_{0.2}$Mn$_{0.2}$O$_2$ and LiNbO$_3$ layers, caused by Ni^{2+} ions diffusion from LiNi$_{0.6}$Co$_{0.2}$Mn$_{0.2}$O$_2$ in the LiNbO$_3$ layer. The electrochemical tests showed that LiNbO$_3$/LiNi0.6Co0.2Mn0.2O2 electrode possesses enhanced stability and

mitigated the impedance increase after cycling compared to bare $LiNi_{0.6}Co_{0.2}Mn_{0.2}O_2$ electrodes.

Post-mortem analyses revealed the stability of the $LiNbO_3/LiNi_{0.6}Co_{0.2}Mn_{0.2}O_2$ interface and showed the elemental distribution in the CEI of both thin-film electrodes. The $LiNbO_3$ layer was found to maintain a compact morphology and effectively suppress cation-mixing, resist HF attack and restrain electrolyte decomposition, leading to an alleviated CEI film growth. The residuals unfavorable to Li-ion transport were detected in fewer amounts at the surface of $LiNbO_3/LiNi_{0.6}Co_{0.2}Mn_{0.2}O_2$ electrodes. This work presents a simple solution to isolate active material from carbon additives and binders. The interaction between Ni-rich $LiNi_{0.6}Co_{0.2}Mn_{0.2}O_2$ cathode and $LiNbO_3$, as well as the CEI film formation between the electrode and electrolyte, was demonstrated. More information on interfacial behavior during cycling can be obtained by more advanced characterization methods, such as in situ atomic-scale techniques. Considering the $LiNbO_3$ is a promising solid-state electrolyte with high ionic conductivity and a wide stability window, the present work also contributes to the development of stable all-solid-state Li-ion batteries. Eqs. ((2), 3.1), (3.2), ((4), (5.1), (5.2), (5.3), (5.4), (5.5))

Declaration of Competing Interest

The authors declare no known competing financial interests or personal relationships that could have appeared to influence the work reported in this paper.

Credit authorship contribution statement

Ming Jiang: Conceptualization, Investigation, Validation, Formal analysis, Writing – original draft. **Xiaochao Wu:** Investigation, Validation, Formal analysis. **Qian Zhang:** Investigation, Validation, Formal analysis. **Dmitri L. Danilov:** Supervision, Writing – review & editing. **Rüdiger-A. Eichel:** Project administration. **Peter H.L. Notten:** Conceptualization, Supervision, Writing – review & editing.

Acknowledgments

Supplementary materials

Supplementary material associated with this article can be found, in the online version, at doi:10.1016/j.electacta.2021.139316.

References

[1] R. Schmuch, R. Wagner, G. Hörpel, T. Placke, M. Winter, Performance and cost of materials for lithium-based rechargeable automotive batteries, Nat. Energy 3 (2018) 267–278.

[2] S. Natarajan, V. Aravindan, Burgeoning prospects of spent lithium-ion batteries in multifarious applications, Adv. Energy Mater. 8 (2018) 1802303.

[3] P. Teichert, G.G. Eshetu, H. Jahnke, E. Figgemeier, Degradation and aging routes of Ni-rich cathode based Li-Ion batteries, Batteries 6 (2020) 8.

[4] L. Liang, W. Zhang, F. Zhao, D.K. Denis, F.u. Zaman, L. Hou, C. Yuan, Surface/interface structure degradation of ni-rich layered oxide cathodes toward lithium-ion batteries: fundamental mechanisms and remedying strategies, Adv. Mater. Interfaces 7 (2019) 1901749.

[5] X. Wang, Y.L. Ding, Y.P. Deng, Z. Chen, Ni-rich/co-poor layered cathode for automotive Li-ion batteries: promises and challenges, Adv. Energy Mater. 10 (2020) 1903864.

[6] J. Kim, H. Cha, H. Lee, P. Oh, J. Cho, Surface and interfacial chemistry in the nickel-rich cathode materials, Batter. Supercaps 3 (2020) 309–322.

[7] M. Jiang, Q. Zhang, X. Wu, Z. Chen, D.L. Danilov, R.A. Eichel, P.H.L. Notten, Synthesis of Ni-Rich layered-oxide nanomaterials with enhanced Li-Ion diffusion pathways as high-rate cathodes for Li-Ion batteries, ACS Appl. Energy Mater. 3 (2020) 6583–6590.

[8] I. Hamam, N. Zhang, A. Liu, M.B. Johnson, J.R. Dahn, Study of the reactions between ni-rich positive electrode materials and aqueous solutions and their relation to the failure of Li-ion cells, J. Electrochem. Soc. 167 (2020) 130521.

[9] W. Liu, X. Li, D. Xiong, Y. Hao, J. Li, H. Kou, B. Yan, D. Li, S. Lu, A. Koo, K. Adair, X. Sun, Significantly improving cycling performance of cathodes in lithium ion batteries: The effect of Al_2O_3 and $LiAlO_2$ coatings on $LiNi_{0.6}Co_{0.2}Mn_{0.2}O_2$, Nano Energy 44 (2018) 111–120.

[10] Y. Li, X. Liu, D. Ren, H. Hsu, G.-L. Xu, J. Hou, L. Wang, X. Feng, L. Lu, W. Xu, Y. Ren, R. Li, X. He, K. Amine, M. Ouyang, Toward a high-voltage fast-charging pouch cell with TiO_2 cathode coating and enhanced battery safety, Nano Energy 71 (2020) 104643.

[11] D. Hu, Y. Su, L. Chen, N. Li, L. Bao, Y. Lu, Q. Zhang, J. Wang, S. Chen, F. Wu, The mechanism of side reaction induced capacity fading of Ni-rich cathode materials for lithium ion batteries, J. Energy Chem. 58 (2020) 1–8.

[12] K. Liu, Q. Zhang, S. Dai, W. Li, X. Liu, F. Ding, J. Zhang, Synergistic effect of F(-) doping and lif coating on improving the high-voltage cycling stability and rate capacity of $LiNi_{0.5}Co_{0.2}Mn_{0.3}O_2$ cathode materials for lithium-ion batteries, ACS Appl. Mater. Interfaces 10 (2018) 34153–34162.

[13] H.H. Sun, J.Y. Hwang, C.S. Yoon, A. Heller, C.B. Mullins, Capacity degradation mechanism and cycling stability enhancement of AlF_3-coated nanorod gradient $Na[Ni_{0.65}Co_{0.08}Mn_{0.27}]O_2$ cathode for sodium-ion batteries, ACS Nano 12 (2018) 12912–12922.

[14] Q. Gan, N. Qin, Z. Wang, Z. Li, Y. Zhu, Y. Li, S. Gu, H. Yuan, W. Luo, L. Lu, Z. Xu, Z. Lu, Revealing mechanism of Li_3PO_4 Coating suppressed surface oxygen release for commercial Ni-Rich layered cathodes, ACS Appl. Energy Mater. 3 (2020) 7445–7455.

[15] B. Song, W. Li, S.M. Oh, A. Manthiram, Long-life nickel-rich layered oxide cathodes with a uniform Li_2ZrO_3 surface coating for lithium-ion batteries, ACS Appl. Mater. Interfaces 9 (2017) 9718–9725.

[16] Y.J. Kim, R. Rajagopal, S. Kang, K.S. Ryu, Novel dry deposition of $LiNbO_3$ or Li_2ZrO_3 on $LiNi_{0.6}Co_{0.2}Mn_{0.2}O_2$ for high performance all-solid-state lithium batteries, Chem. Eng. J. 386 (2020) 123975.

[17] Q. Fan, S. Yang, J. Liu, H. Liu, K. Lin, R. Liu, C. Hong, L. Liu, Y. Chen, K. An, P. Liu, Z. Shi, Y. Yang, Mixed-conducting interlayer boosting the electrochemical performance of Ni-rich layered oxide cathode materials for lithium ion batteries, J. Power Sources 421 (2019) 91–99.

[18] Q. Ran, H. Zhao, X. Shu, Y. Hu, S. Hao, Q. Shen, W. Liu, J. Liu, M. Zhang, H. Li, X. Liu, Enhancing the electrochemical performance of Ni-Rich layered oxide cathodes by combination of the gradient doping and dual-conductive layers coating, ACS Appl. Energy Mater. 2 (2019) 3120–3130.

[19] S. Yang, Q. Fan, Z. Shi, L. Liu, J. Liu, X. Ke, J. Liu, C. Hong, Y. Yang, Z. Guo, Superior stability secured by a four-phase cathode electrolyte interface on a Ni-Rich Cathode for lithium ion batteries, ACS Appl. Mater. Interfaces 11 (2019) 36742–36750.

[20] S. Chen, T. He, Y. Su, Y. Lu, L. Bao, L. Chen, Q. Zhang, J. Wang, R. Chen, F. Wu, Ni-Rich $LiNi_{0.8}Co_{0.1}Mn_{0.1}O_2$ oxide coated by dual-conductive layers as high performance cathode material for lithium-ion batteries, ACS Appl. Mater. Interfaces 9 (2017) 29732–29743.

[21] T. Teranishi, M. Inohara, J. Kano, H. Hayashi, A. Kishimoto, K. Yoda, H. Motobayashi, Y. Tasaki, Synthesis of nano-crystalline $LiNbO_3$-decorated $LiCoO_2$ and resulting high-rate capabilities, Solid State Ionics 314 (2018) 57–60.

[22] M. Gellert, K.I. Gries, J. Sann, E. Pfeifer, K. Volz, B. Roling, Impedance spectroscopic study of the charge transfer resistance at the interface between a $LiNi_{0.5}Mn_{1.5}O_4$ high-voltage cathode film and a $LiNbO_3$ coating film, Solid State Ion. 287 (2016) 8–12.

[23] Z.J. Zhang, S.L. Chou, Q.F. Gu, H.K. Liu, H.J. Li, K. Ozawa, J.Z. Wang, Enhancing the high rate capability and cycling stability of $LiMn_2O_4$ by coating of solid-state electrolyte $LiNbO_3$, ACS Appl. Mater. Interfaces 6 (2014) 22155–22165.

[24] J. Syzdek, M. Marcinek, R. Kostecki, Electrochemical activity of carbon blacks in $LiPF_6$-based organic electrolytes, J. Power Sources 245 (2014) 739–744.

[25] N.D. Phillip, R.E. Ruther, X. Sang, Y. Wang, R.R. Unocic, A.S. Westover, C. Daniel, G.M. Veith, Synthesis of Ni-Rich thin-film cathode as model system for lithium ion batteries, ACS Appl. Energy Mater. 2 (2019) 1405–1412.

[26] S. Lobe, C. Dellen, M. Finsterbusch, H.G. Gehrke, D. Sebold, C.L. Tsai, S. Uhlenbruck, O. Guillon, Radio frequency magnetron sputtering of $Li_7La_3Zr_2O_{12}$ thin films for solid-state batteries, J. Power Sources 307 (2016) 684–689.

[27] Z.P.W. Shravan Suresh, S.F. Bartolucci, S. Basu, R. Mukherjee, T. Gupta, P. Hundekar, Y. Shi, T.M. Lu, N. Koratkar, Protecting silicon film anodes in lithium-ion batteries using an atomically thin graphene drape, ACS Nano 11 (2017) 5051–5061.

[28] Z. Yu, H. Xu, G. Zhu, D.L. Yan, A. Yu, Binary lithium titanate-titania nanocomposite thin-film electrodes for electrochemical energy storage, Energy Technol. 4 (2016) 798–803.

[29] G. Tan, F. Wu, J. Lu, R. Chen, L. Li, K. Amine, Controllable crystalline preferred orientation in Li-Co-Ni-Mn oxide cathode thin films for all-solid-state lithium batteries, Nanoscale 6 (2014) 10611–10622.

[30] J.F.M. Oudenhoven, Deposition and characterization of thin films for 3D lithium-ion micro-batteries, Doctoral dissertation, Eindhoven University of Technology, 2011.

[31] S. Moitzheim, B. Put, P.M. Vereecken, Advances in 3D thin-film Li-ion batteries, Adv. Mater. Interfaces 6 (2019) 1900805.

[32] Y. Zhu, X. He, Y. Mo, First principles study on electrochemical and chemical stability of solid electrolyte–electrode interfaces in all-solid-state Li-ion batteries, J. Mater. Chem. A 4 (2016) 3253–3266.

[33] J. Fu, D. Mu, B. Wu, J. Bi, H. Cui, H. Yang, H. Wu, F. Wu, Electrochemical properties of the $LiNi_{0.6}Co_{0.2}Mn_{0.2}O_2$ cathode material modified by lithium tungstate under high voltage, ACS Appl. Materi. Interfaces 10 (2018) 19704–19711.

[34] X. Ju, H. Huang, W. He, H. Zheng, P. Deng, S. Li, B. Qu, T. Wang, Surfactant-assisted synthesis of high energy {010} facets beneficial to Li-Ion transport

kinetics with layered LiNi$_{0.6}$Co$_{0.2}$Mn$_{0.2}$O$_2$, ACS Sustain. Chem. Eng. 6 (2018) 6312–6320.

[35] K. Li, D. Xue, Estimation of electronegativity values of elements in different valence states, J. Phys. Chem. A 110 (2006) 11332–11337.

[36] J. Zhao, W. Zhang, A. Huq, S.T. Misture, B. Zhang, S. Guo, L. Wu, Y. Zhu, Z. Chen, K. Amine, F. Pan, J. Bai, F. Wang, *In situ* probing and synthetic control of cationic ordering in Ni-rich layered oxide cathodes, Adv. Energy Mater. 7 (2017) 1601266.

[37] W. Li, J.N. Reimers, J.R. Dahn, *In situ* X-ray diffraction and electrochemical studies of Li$_{l-x}$NiO$_2$, Solid State Ion. 67 (1993) 123–130.

[38] W. Zhao, G. Zheng, M. Lin, W. Zhao, D. Li, X. Guan, Y. Ji, G.F. Ortiz, Y. Yang, Toward a stable solid-electrolyte-interfaces on nickel-rich cathodes: LiPO$_2$F$_2$ salt–type additive and its working mechanism for LiNi$_{0.5}$Mn$_{0.25}$Co$_{0.25}$O$_2$ cathodes, J. Power Sources 380 (2018) 149–157.

[39] J. Kim, H. Ma, H. Cha, H. Lee, J. Sung, M. Seo, P. Oh, M. Park, J. Cho, A highly stabilized nickel-rich cathode material by nanoscale epitaxy control for high-energy lithium-ion batteries, Energy Environ. Sci. 11 (2018) 1449–1459.

[40] H. Chen, L. Xiao, H. Chen, Y. Zhu, K. Xiang, H. Liao, Construction of core-shell Li$_3$PO$_4$@LiNi$_{0.5}$Co$_{0.2}$Mn$_{0.3}$O$_2$ cathode with improved cycling stability for lithium ion batteries, Electrochim. Acta 344 (2020) 136142.

[41] Y. Zhang, Z.B. Wang, F.D. Yu, L.F. Que, M.J. Wang, Y.F. Xia, Y. Xue, J. Wu, Studies on stability and capacity for long-life cycle performance of Li(Ni$_{0.5}$Co$_{0.2}$Mn$_{0.3}$)O$_2$ by Mo modification for lithium-ion battery, J. Power Sources 358 (2017) 1–12.

[42] J. Kim, J. Lee, H. Ma, H.Y. Jeong, H. Cha, H. Lee, Y. Yoo, M. Park, J. Cho, Controllable solid electrolyte interphase in nickel-rich cathodes by an electrochemical rearrangement for stable lithium-ion batteries, Adv. Mater. 30 (2018) 17043091–17043099.

[43] S. Fang, D. Jackson, M.L. Dreibelbis, T.F. Kuech, R.J. Hamers, Anode-originated SEI migration contributes to formation of cathode-electrolyte interphase layer, J.f Power Sources 373 (2018) 184–192.

[44] H. Lee, H.S. Lim, X. Ren, L. Yu, M.H. Engelhard, K.S. Han, J. Lee, H.T. Kim, J. Xiao, J. Liu, W. Xu, J.G. Zhang, Detrimental effects of chemical crossover from the lithium anode to cathode in rechargeable lithium metal batteries, ACS Energy Lett. 3 (2018) 2921–2930.

[45] J. Langdon, A. Manthiram, Crossover effects in batteries with high-nickel cathodes and lithium-metal anodes, Adv. Funct. Mater. 31 (2021) 2010267.

[46] T. Kim, L.K. Ono, N. Fleck, S.R. Raga, Y. Qi, Transition metal speciation as a degradation mechanism with the formation of a solid-electrolyte interphase (SEI) in Ni-rich transition metal oxide cathodes, J. Mater. Chem. A 6 (2018) 14449–14463.

[47] J.M. Lim, N.S. Luu, K.Y. Park, M.T.Z. Tan, S. Kim, J.R. Downing, K. He, V.P. Dravid, M.C. Hersam, Enhancing nanostructured nickel-rich lithium-ion battery cathodes via surface stabilization, J. Vac. Sci. Technol. A 38 (2020) 0632101–0632109.

[48] D. Li, H. Li, D.L. Danilov, L. Gao, X. Chen, Z. Zhang, J. Zhou, R.-A. Eichel, Y. Yang, P.H.L. Notten, Degradation mechanisms of C$_6$/LiNi$_{0.5}$Mn$_{0.3}$Co$_{0.2}$O$_2$ Li-ion batteries unraveled by non-destructive and post-mortem methods, J. Power Sources 416 (2019) 163–174.

[49] Y. Shi, M. Zhang, C. Fang, Y.S. Meng, Urea-based hydrothermal synthesis of LiNi$_{0.5}$Co$_{0.2}$Mn$_{0.3}$O$_2$ cathode material for Li-ion battery, J. Power Sources 394 (2018) 114–121.

[50] K. Kumai, H. Miyashiro, Y. Kobayashi, K. Takei, R. Ishikawa, Gas generation mechanism due to electrolyte decomposition in commercial lithium-ion cell, J. Power Sources 81 (1999) 715–719.

[51] B. Ravdel, K.M. Abraham, R. Gitzendanner, J. DiCarlo, B. Lucht, C. Campion, Thermal stability of lithium-ion battery electrolytes, J. Power Sources 119-121 (2003) 805–810.

[52] C.L. Campion, W. Li, B.L. Lucht, Thermal decomposition of LiPF$_6$-based electrolytes for lithium-ion batteries, J. Electrochem. Soc. 152 (2005) A2327.

[53] W. Li, B.L. Lucht, Lithium-ion batteries: thermal reactions of electrolyte with the surface of metal oxide cathode particles, J. Electrochem. Soc. 153 (2006) A1617.

[54] P. Niehoff, M. Winter, Composition and growth behavior of the surface and electrolyte decomposition layer of/on a commercial lithium ion battery Li$_x$Ni$_{1/3}$Mn$_{1/3}$Co$_{1/3}$O$_2$ cathode determined by sputter depth profile X-ray photoelectron spectroscopy, Langmuir 29 (2013) 15813–15821.

[55] Q. Li, Y. Wang, X. Wang, X. Sun, J.N. Zhang, X. Yu, H. Li, Investigations on the fundamental process of cathode electrolyte interphase formation and evolution of high-voltage cathodes, ACS Appl. Mater. Interfaces 12 (2020) 2319–2326.

[56] G. Liu, N. Xu, Y. Zou, K. Zhou, X. Yang, T. Jiao, W. Yang, Y. Yang, J. Zheng, Stabilizing Ni-Rich LiNi$_{0.83}$Co$_{0.12}$Mn$_{0.05}$O$_2$ with cyclopentyl isocyanate as a novel electrolyte additive, ACS Appl. Mater. Interfaces 13 (2021) 12069–12078.